**Supplemental information**

Synthesis of *C*-glycosides by Ti-catalyzed stereoselective glycosyl radical functionalization

Yi Jiang, Quanquan Wang, Xinglong Zhang, and Ming Joo Koh

dissolved in 0.5 mL dry THF. The vial was tightly capped and removed from the glovebox. The mixture was allowed to vigorously stir at room temperature for 16 h. After the reaction was complete, the volatiles were evaporated and the residues were purified by flash silica gel column chromatography (eluent: hexanes : EtOAc = 2:1) gave the pure product **5h** as a colorless oil (α only, 42.3 mg, 63% yield). The conversion of **18** was observed to be <10% and the corresponding alkylated product **19b** was detected in <5% yield.

6.4 Cyclic voltammetry studies

Cyclic voltammetry (CV) experiments were conducted in a 10 mL glass vial fitted with a glassy carbon working electrode (3 mm in diameter, BASi), a Ag/AgCl reference electrode, and a platinum tablet counter electrode. The solution of interest was sparged with nitrogen for 3−5 minutes before data collection. Current was reported in μA, while all potentials were reported in V. Cyclic voltammograms of **3a−3d** and Cp*TiCl₃ (10 mM) in MeCN (0.1 M n-Bu₄NClO₄) with a scan rate of 100 mV/s are shown below.
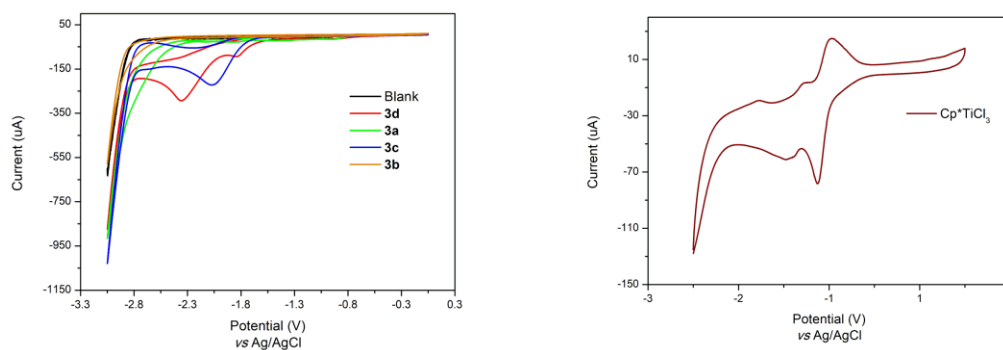
7. Computational studies

7.1 Computational methods

Kohn-Sham Density functional theory (KS-DFT) calculations were performed with *Gaussian 16* rev. B.01.[1] Geometry optimizations were performed using the B3LYP hybrid functional[2–5] with Grimme's D3 dispersion correction with Becke-Jonson damping[6] (herein denoted B3LYP-D3BJ) and the def2-SVP[7] Karlsruhe-family basis

set. Minima and transition structures on the potential energy surface (PES) were confirmed using harmonic frequency analysis at the same level of theory, showing respectively zero and one imaginary frequency. Single point (SP) corrections were performed using B3LYP-D3BJ and def2-TZVP[7] basis set for all atoms. The SMD implicit continuum solvation model[8] was used to account for the effect of tetrahydrofuran (THF) solvent on the computed Gibbs energy profile. Gibbs energies were evaluated at the room temperature, using a quasi-RRHO treatment of vibrational entropies,[9] using the GoodVibes code.[10] Vibrational entropies of frequencies below 100 cm^{-1} were obtained according to a free rotor description, using a smooth damping function to interpolate between the two limiting descriptions. The free energies were further corrected using standard concentration of 1 mol/L, which were used in solvation calculations. Unless otherwise stated, the final SMD (THF)-B3LYP-D3BJ/def2-TZVP//B3LYP-D3BJ/def2-SVP Gibbs energies are used for discussion throughout. *All Gibbs energy values in the text and figures are quoted in kcal mol^{-1}.*

For species involving open-shell characteristics, including doublet radicals, radical ions and closed-shell diradicals, we performed above-mentioned DFT methodologies using the unrestricted formalism of Kohn-Sham theory (UKS). Wavefunction stability in the cases of closed-shell diradicals were checked using Gaussian keyword "*stable=opt, guess=mix*". The eigenvalues of the spin operator **S^2** after annihilation of spin contamination were checked to ensure that they comply with the expected value of *S(S+1) = 0.75* for a doublet wavefunction and *S(S+1) = 0* for closed shell diradical, indicating that spin contamination is not a problem for the present methodology.

Non-covalent interactions (NCIs) were analyzed using NCIPLOT[11] calculations. The *.wfn* files for NCIPLOT were generated at B3LYP-D3BJ/def2-SVP level of theory. NCI indices calculated with NCIPLOT were visualized at a gradient isosurface value of *s = 0.5* au. These are colored according to the sign of the second eigenvalue (λ_2) of the Laplacian of the density ($\nabla^2\rho$) over the range of -0.1 (blue = attractive) to +0.1 (red = repulsive). All molecular structures and molecular orbitals were visualized

using *PyMOL* software.[12] Geometries of all optimized structures (in *.xyz* format with their associated energy in Hartrees) are included in a separate folder named *structures_xyz* with an associated README file. All these data have been deposited with this Supporting Information.

7.2 Model simplification and conformational considerations

Mannosyl chloride **3f** and ᵗBu–Cl **20** are used in computational modelling (Scheme S3 a)). The mannosyl radical generated from the homolytic cleavage of mannosyl chloride adopts a chair-like conformer (Scheme S3, b)), as described in literature by computational studies.[13,14]
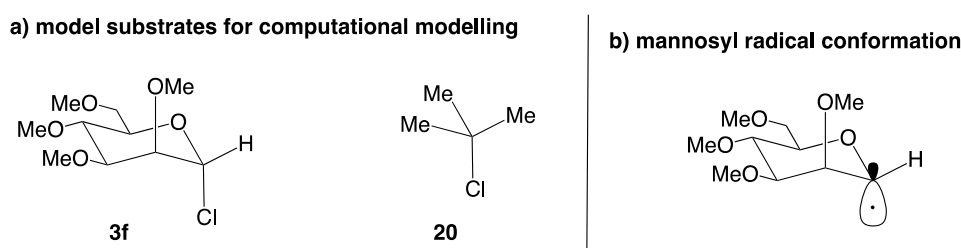
Scheme S3. a) Model substrates used in computational modelling, and b) chair-like conformation for mannosyl radical.

7.3 Gibbs energy profile without Ti-participation for radical addition step

Figure S1 shows the overall Gibbs energy profiles for the Ti-catalyzed radical alkylation reaction. The reaction energy profiles compare the relative reactivities for ᵗBu–Cl (pathway in blue) vs glycosyl chloride (pathway in black). The overall transformation proceeds with first the generation of radical, followed by radical addition to the acrylamide, and finally the reduction of the radical intermediate to the neutral product.

The DFT-optimized key TSs are shown in Figure S2. The generation of ᵗBu• radical (**TS1'**) has a barrier of 9.2 kcal mol⁻¹, which is 2.7 kcal mol⁻¹ higher than the generation of the glycosyl/mannosyl radical (**TS1**, at 6.5 kcal mol⁻¹). This implies a kinetic preference for the generation of glycosyl/mannosyl radical over ᵗBu• radical by *ca.* 95 times at room temperature, using simple transition state theory. This step is

exergonic as the radicals formed have lower Gibbs energy than the starting material. In addition, this step is irreversible, as the subsequent radical addition (step from R$^{\bullet}$ to acrylamide adduct via **TS2/TS2'**) has lower barriers than reversible addition of radical to Cp*TiCl$_3$ (step from R$^{\bullet}$ back to substrate **iii** and **iii'** via **TS1/TS1'**): for the glycosyl/mannosyl pathway, the forward barrier is 8.8 kcal mol^{-1} while the reverse barrier is 9.9 kcal mol^{-1}; for the ^{t}BuCl pathway, the forward barrier is 10.5 kcal mol^{-1} while the reverse barrier is 13.6 kcal mol^{-1}.
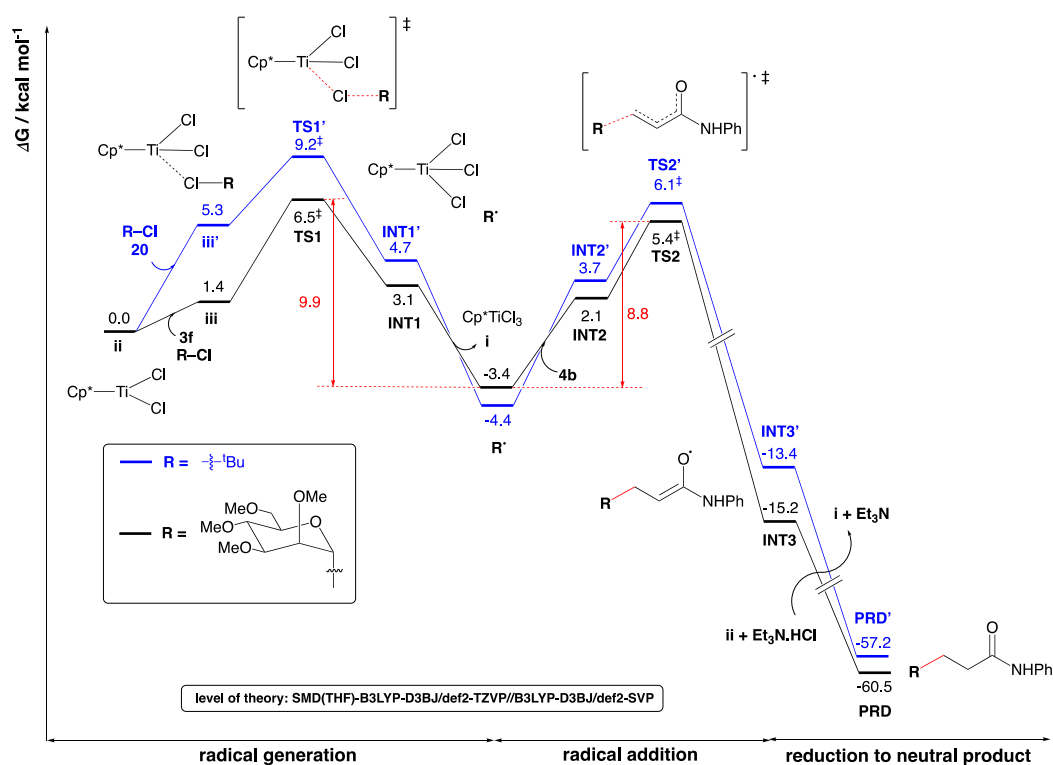

Figure S1. Overall Gibbs energy profile. Relative Gibbs energies are given in kcal mol^{-1}.

For the radical addition to acrylamide **4b**, in the absence of any coordination of acrylamide **4b** to Ti-catalyst, which could act as a Lewis acid (considered in section 6.4), the addition of glycosyl/mannosyl radical to acrylamide has a barrier of is 8.8 kcal mol^{-1} (**TS2**) whereas the addition of ^{t}Bu$^{\bullet}$ radical to acrylamide has a barrier of 10.5 kcal mol^{-1} (**TS2'**). The activation energy difference, $\Delta\Delta G^{\ddagger} = 1.7$ kcal mol^{-1} translates to a kinetic preference for glycosyl/mannosyl radical addition over ^{t}Bu$^{\bullet}$ radical addition to acrylamide by 18 times at room temperature. We will see that with

Ti-catalyst coordination to acrylamide, the radical addition step is not the overall rate-determining step and instead the radical generation step is the overall rate-determining step (*vide infra*).
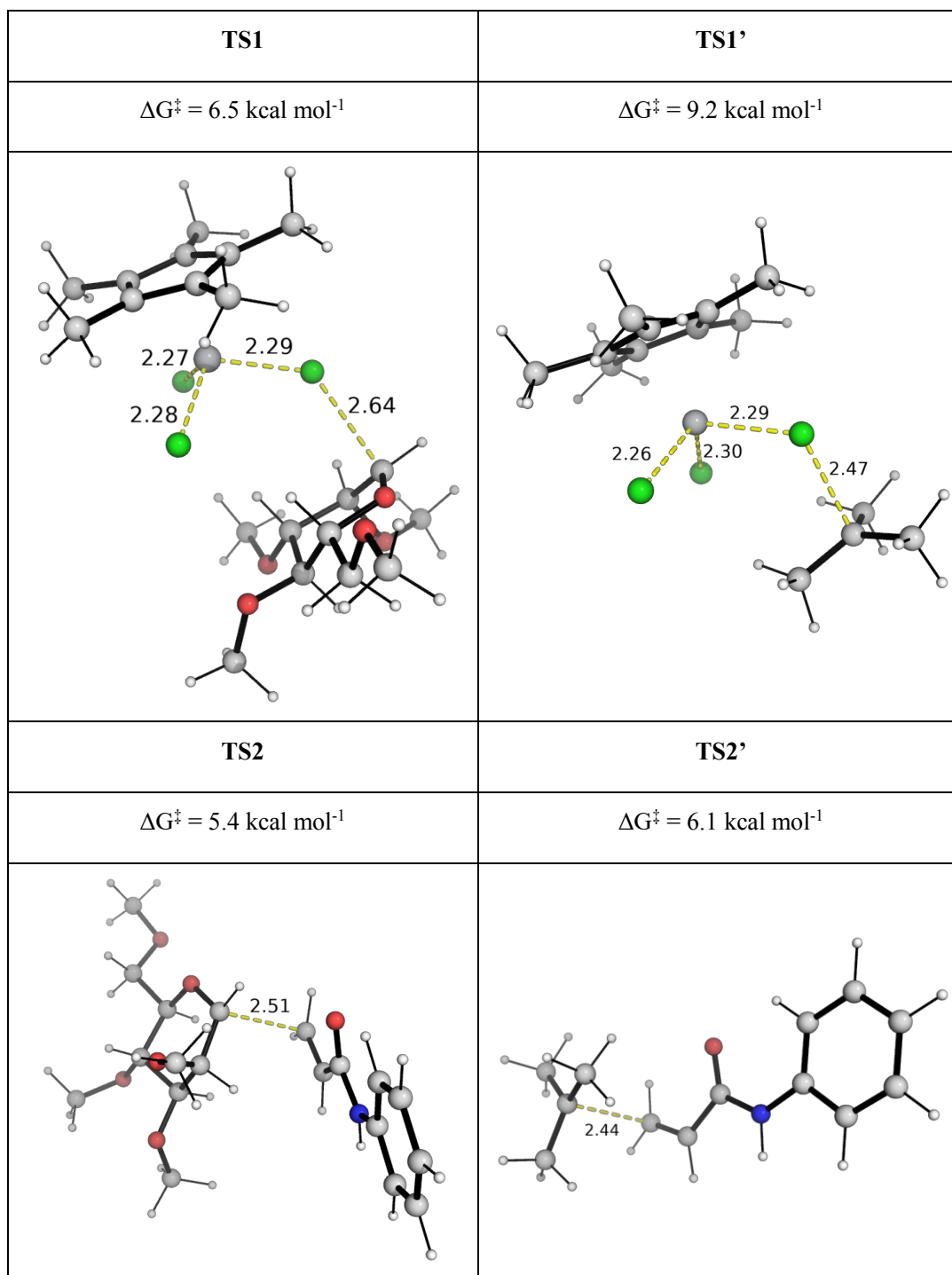
TS1	TS1'
$\Delta G^{\ddagger} = 6.5$ kcal mol^{-1}	$\Delta G^{\ddagger} = 9.2$ kcal mol^{-1}
TS2	**TS2'**
$\Delta G^{\ddagger} = 5.4$ kcal mol^{-1}	$\Delta G^{\ddagger} = 6.1$ kcal mol^{-1}

Figure S2. DFT optimized TS structures for the radical generation step (**TS1** and **TS1'**) and the radical addition to acrylamide (**TS2** and **TS2'**).

The reduction of the radical adduct **INT3/INT3'** by Cp*Ti$^{(III)}$Cl$_2$ and subsequent

protonation of the resultant enolate to give the final neutral product is highly exergonic and irreversible.

7.4 Gibbs energy profile with Ti-participation for radical addition step

The radical generation step in this case is the same as discussed in section 6.3. For the addition of the resultant radical to the Cp*Ti$^{(III)}$Cl$_2$-coordinated acrylamide, no transition state structures were found – the optimization of reactant complex (with the forming C–C bond separation of > 3.5Å) yields the product directly, indicating no barrier for the radical addition to the Ti(III)-activated acrylamide.

We further performed relaxed potential energy surface (PES) scans along the forming C–C bond and the result is shown in Figure S3, note that the C–C bond length range scanned cover the bond distances of **TS2** (2.51Å) and **TS2'** (2.44Å) shown in Figure S2. From Figure S3, we can see that no activation barrier exists for the addition of glycosyl/mannosyl radical to the Ti(III)-activated acrylamide. For the addition of $^{t}Bu^{•}$ radical to the Ti(III)-activated acrylamide, there exists a small barrier for the complex formation (point 1 to point 2 in Figure S2b)). However, this barrier is much smaller compared to the transition state for radical generation (**TS1'**), shown in Figure S1.
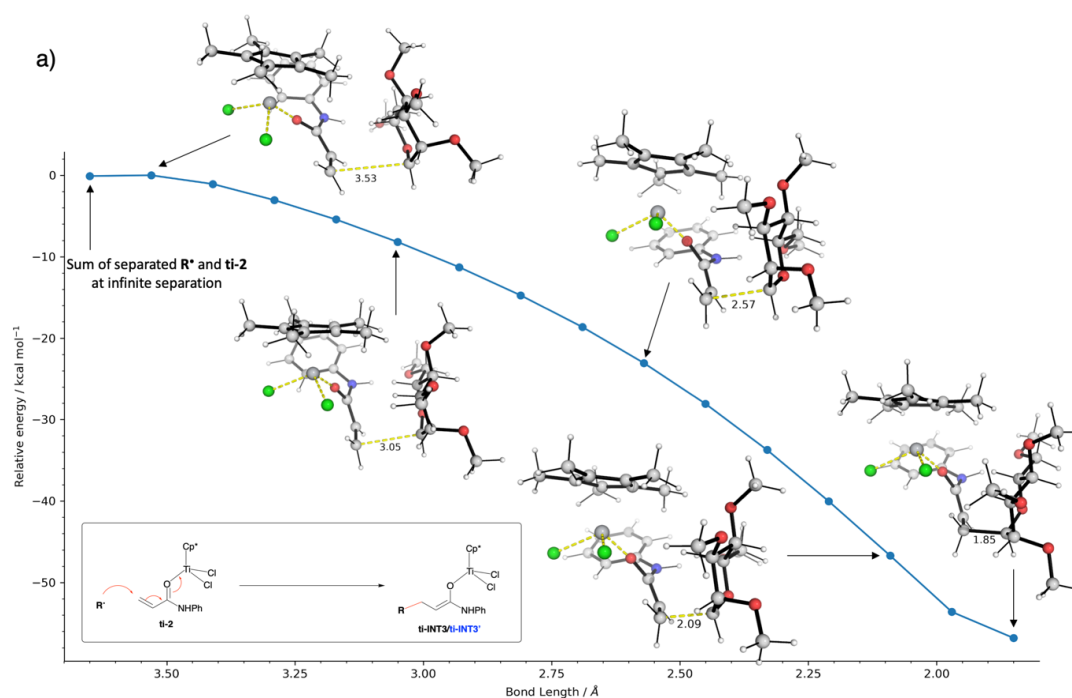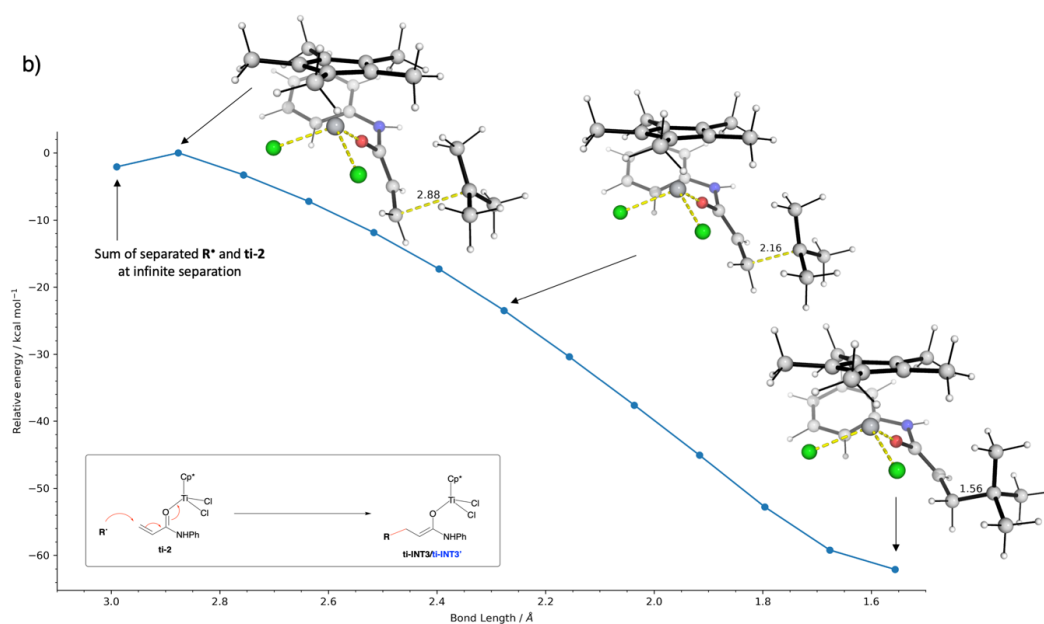
Figure S3. Relaxed potential energy surface (PES) scan in gas phase using UB3LYP-D3BJ/def2-SVP (*guess=mix*) for openshell-diradical system for a) the addition of glycosyl/mannosyl radical and b) the addition of tBu radical to Cp*Ti$^{(III)}$Cl$_2$-coordinated acrylamide (named **ti-2** herein). Energy values are used without further corrections.

Figure S4 shows the Gibbs energy changes for the radical addition to Ti(III)-activated acrylamide, followed by the reduction to neutral product. We can see that these steps are highly exergonic and irreversible, as a strong C–C bond is formed. As a result of this analysis, we conclude that the rate-limiting step for the present Ti-catalyzed radical alkylation is the generation of radical step (**TS1** vs **TS1'**).
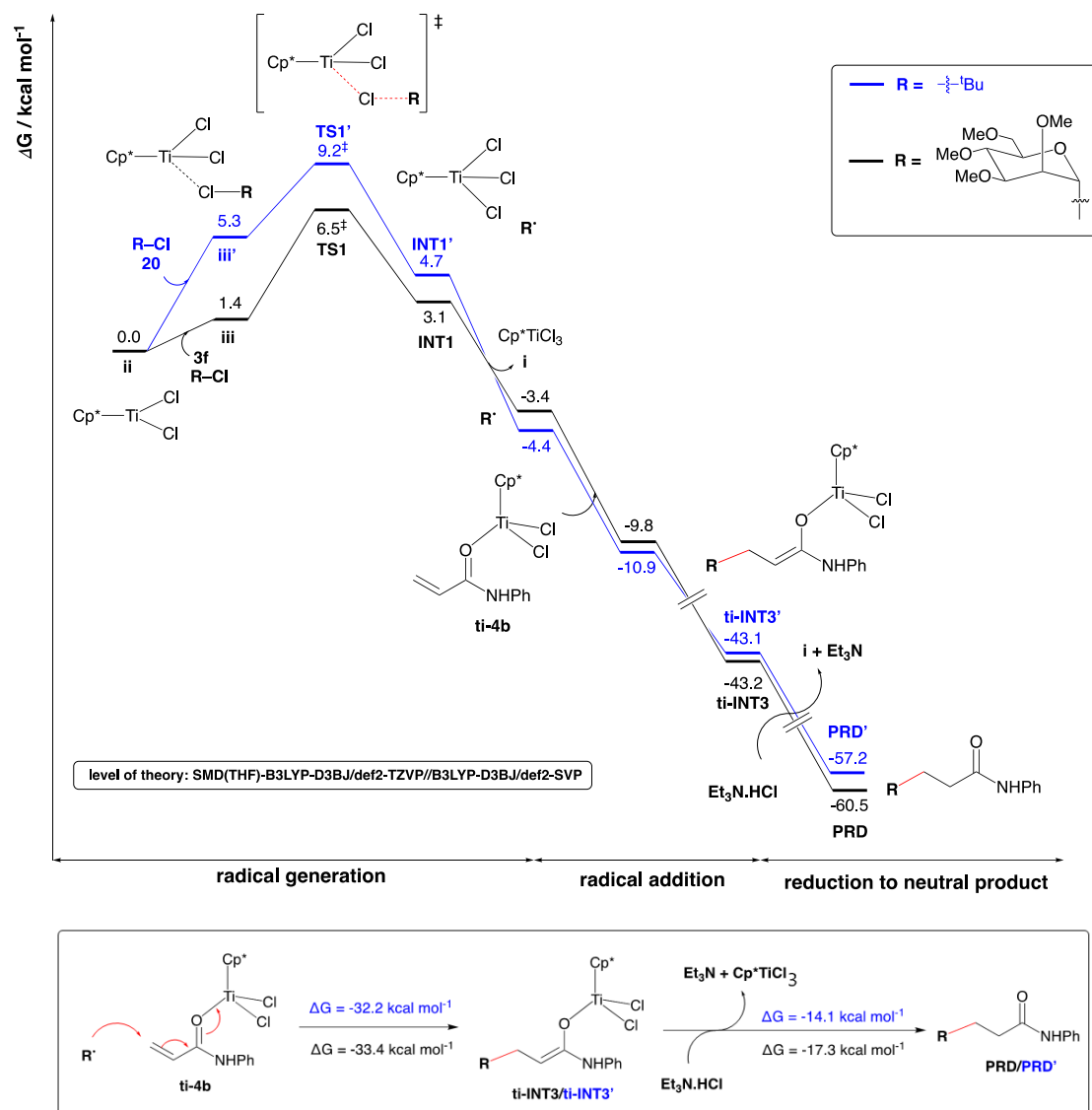
Figure S4. SMD(THF)-UB3LYP-D3BJ/def2-TZVP//UB3LYP-D3BJ/def2-SVP Gibbs energy change for the addition of radical to Ti(III)-coordinated acrylamide.

7.5 C–Cl bond strength and Radical stability

The bond dissociation enthalpies (BDEs) of the substrate can be computed. The corresponding radicals where a chlorine atom is removed were optimized, using unrestricted KS-DFT formalism, in addition to a chlorine atom. The BDE is calculated as

$$\text{BDE (R–Cl)} = H(R^{\bullet}) + H(R^{\bullet}) - H(R\text{–Cl})$$

where H (X) is the enthalpy of chemical species X.

The calculations show that the C–Cl bond strengths in mannosyl chloride and ^{t}BuCl are similar, at 80.4 kcal mol^{-1} and 80.3 kcal mol^{-1}, respectively.

Looking at the spin densities of the mannosyl and ^{t}Bu$^\bullet$ radicals, we can see that the spin density in the former is localized on the anomeric carbon atom where chorine is removed, as well as on the anomeric oxygen atom, which stabilizes the mannosyl radical. On the other hand, the ^{t}Bu$^\bullet$ radical has spin density mostly on the carbon atom from which chlorine is abstracted. The stabilization by anomeric oxygen in mannosyl radical is likely to contribute to the stabilizing of the TS for mannosyl radical generation (**TS1**), resulting in lower activation barrier than ^{t}Bu$^\bullet$ radical generation (**TS1'**).
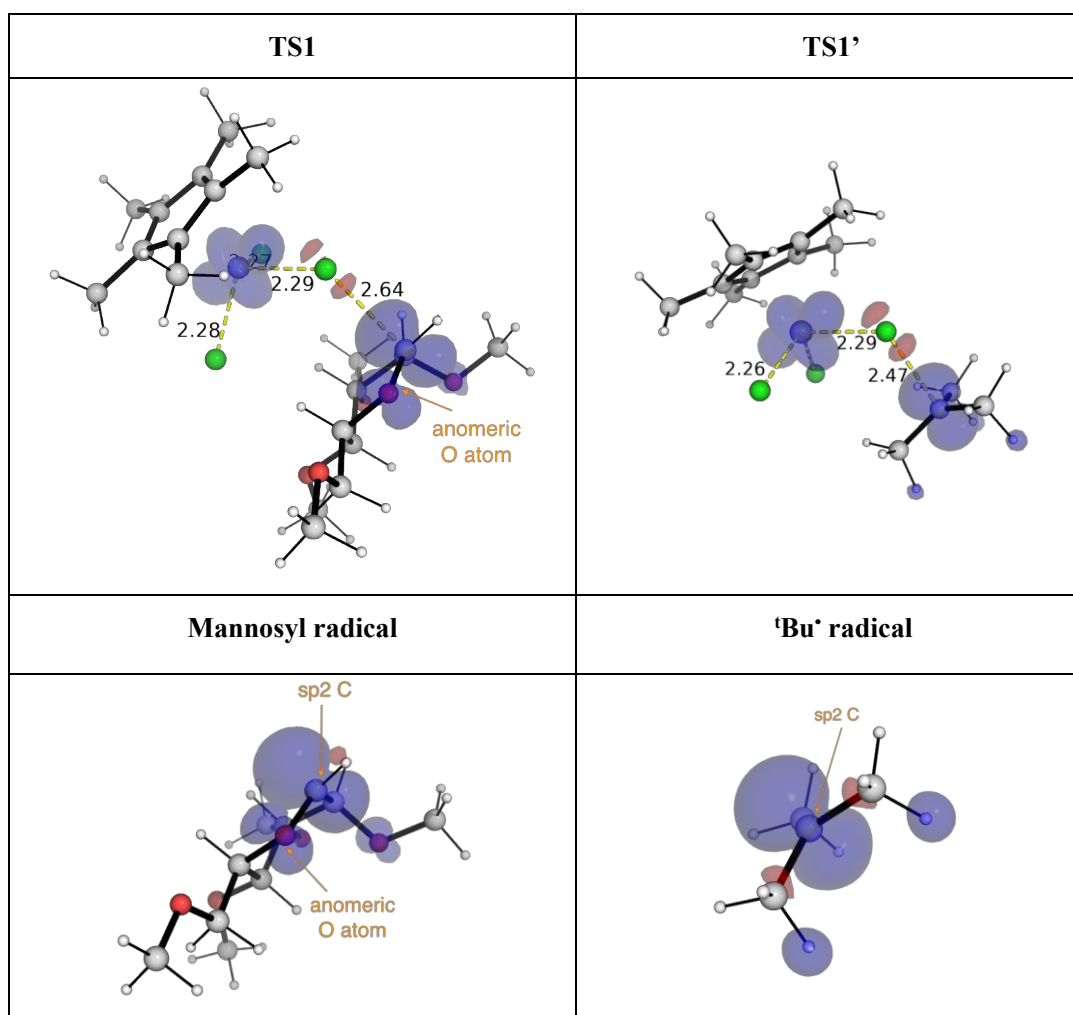

Figure S5. Spin density plots for the transition structures for the generation of mannosyl radical (**TS1**) and *tert*-butyl radical (**TS1'**), as well as for mannosyl radical and ^{t}Bu$^\bullet$ radical at isosurface value of 0.005 au.

7.6 Binding energies

The Gibbs energy change for the binding of glycosyl chloride **3f**, *tert*-butyl chloride **20**, acrylate **4a** and acrylamide **4b** were evaluated and the results are shown in Figure S6.
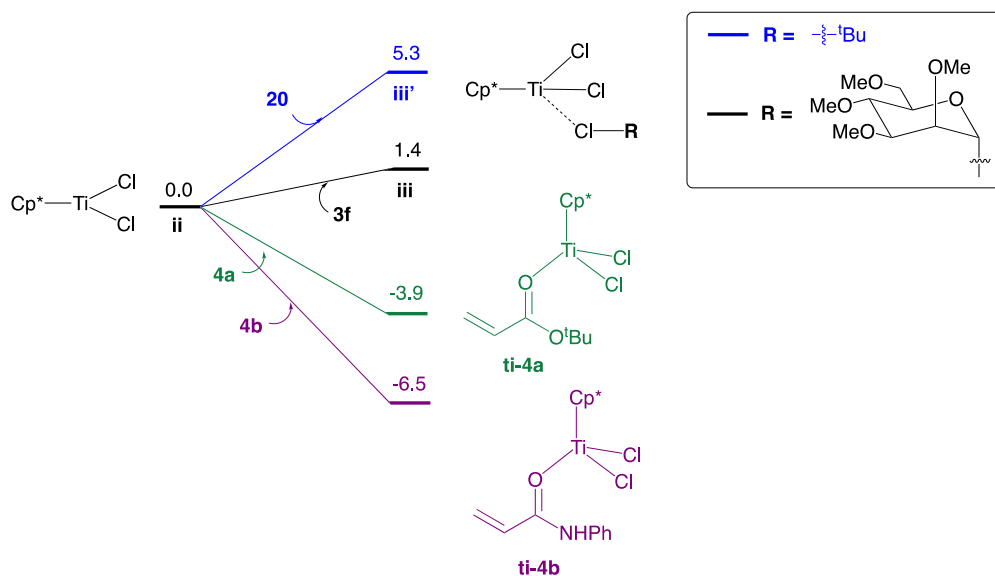

Figure S6. Gibbs energies of reaction (ΔG_r) for the binding of each chemical species to Cp*TiCl$_2$. Values are given in kcal mol^{-1}.

Comparing the binding energies of acrylate **4a** and acrylamide **4b**, we see that in the presence of both species, acrylamide **4b** will preferentially bind to Cp*TiCl$_2$ catalyst over acrylate **4a**, possibly due to the more electron rich nature of acrylamide.

Comparing the binding of glycosyl chloride **3f** and *tert*-butyl chloride **20**, the binding of the former is more favorable. Their singly occupied molecular orbital (SOMO), spin density and non-covalent interactions (NCIs) appear to be similar. It is possible that the binding of glycosyl chloride **3f** gives a more stable complex due to its more favorable CH--Cl non-covalent interaction (NCI) between the CH group of the anomeric carbon and the Cl atom on Cp*TiCl$_2$ (circled in orange, Figure S7) than the NCI between the CH group of the methyl group of *tert*-butyl chloride **20** and the Cl atom on Cp*TiCl$_2$ (circled in orange, Figure S7) as suggested by the shorter CH–Cl distance in **iii** (2.36Å) than in **iii'** (2.66Å).
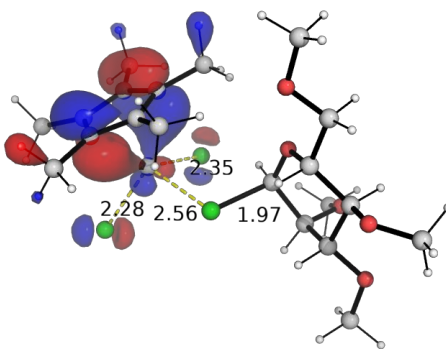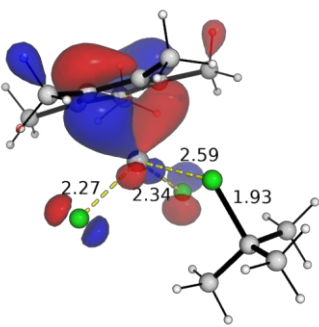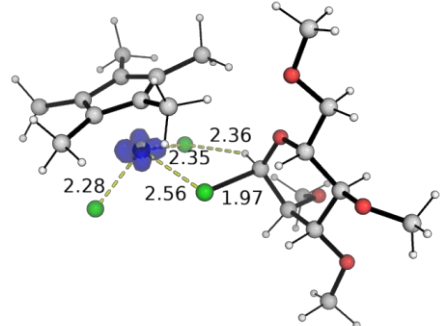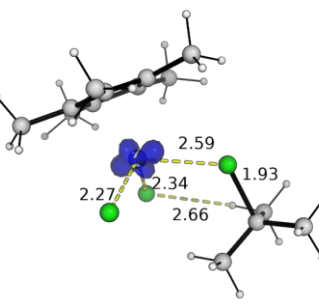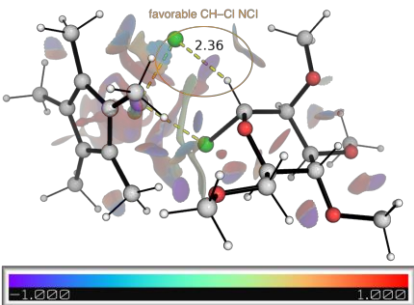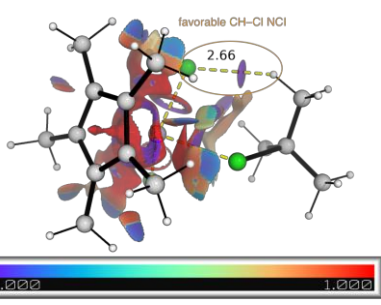
	iii	**iii'**
SOMO		
Spin density plot		
Non-covalent interactions (NCI) plot		

Figure S7. Plots of singly occupied molecular orbital (SOMO), spin density and non-covalent interactions (NCIs) for glycosyl chloride coordinated species **iii** and *tert*-butyl chloride coordinated species **iii'**.

7.7 Optimized structures and absolute energies, zero-point energies

Geometries of all optimized structures have been uploaded to zenodo.org (DOI: 10.5281/zenodo.4876297).

Absolute values (in Hartrees) for SCF energy, zero-point vibrational energy (ZPE), enthalpy and quasi-harmonic Gibbs free energy (at 25ºC/298.15 K) for optimized

structures are given below. Single point corrections in SMD THF using B3LYP-D3BJ/def2-TZVP level of theory are also included.

Structure	E/au	ZPE/au	H/au	T.S/au	qh-G/au	SP SMD(THF)-B3LYP-D3BJ/def2-TZVP
3f	-1228.11276	0.298136	-1227.7952	0.064182	-1227.856406	-1229.162048
3f_radical	-767.973917	0.293565	-767.662	0.061974	-767.721294	-768.8612967
4b	-478.0418	0.160972	-477.87033	0.043071	-477.912412	-478.5851475
cl_radical	-460.006005	0	-460.00364	0.015019	-460.018663	-460.1693831
4a	-424.139369	0.178611	-423.9494	0.043465	-423.992287	-424.6282267
ti-4a	-2583.783389	0.40486	-2583.3488	0.084895	-2583.430251	-2585.120437
20	-617.834462	0.121784	-617.70522	0.033985	-617.739217	-618.1784793
20_radical	-157.698291	0.115668	-157.57528	0.033823	-157.608987	-157.8772053
Et3N	-292.233259	0.204717	-292.01814	0.041414	-292.058876	-292.5640443
Et3N.HCl	-752.936735	0.217374	-752.70719	0.04607	-752.752387	-753.4462825
ti-4b	-2637.689686	0.387051	-2637.2738	0.084821	-2637.354219	-2639.081438
INT2'	-635.749282	0.278047	-635.45258	0.065112	-635.513259	-636.4666674
TS2'	-635.747939	0.278951	-635.45187	0.060005	-635.508774	-636.4660296
INT3'	-635.787759	0.283086	-635.48838	0.057368	-635.543019	-636.5026895
PRD'	-636.441707	0.297008	-636.1286	0.056243	-636.182219	-637.1570993
INT2	-1246.028953	0.452402	-1245.5464	0.092676	-1245.631009	-1247.453595
TS2	-1246.025363	0.452582	-1245.5437	0.090627	-1245.626234	-1247.449656
INT3	-1246.065228	0.455673	-1245.581	0.087488	-1245.661851	-1247.48671
PRD	-1246.720113	0.469903	-1246.2219	0.085683	-1246.301338	-1248.144169
i	-2619.74185	0.226168	-2619.4959	0.066057	-2619.55869	-2620.765433
ii	-2159.592283	0.22385	-2159.35	0.063217	-2159.410307	-2160.461864
iii	-3387.74607	0.520302	-3387.187	0.108829	-3387.28797	-3389.641458
TS1-c2	-3387.736893	0.518484	-3387.1801	0.107315	-3387.279997	-3389.631774

INT1	-3387.742765	0.517875	-3387.1857	0.110467	-3387.287702	-3389.635633
iii-c2	-3387.743851	0.519803	-3387.185	0.109666	-3387.286677	-3389.635573
TS1	-3387.734389	0.517512	-3387.1781	0.110794	-3387.279756	-3389.629838
INT1-c2	-3387.735305	0.517288	-3387.1786	0.113087	-3387.281834	-3389.632017
iii'	-2777.457579	0.346941	-2777.084	0.080627	-2777.160208	-2778.652096
TS1'	-2777.4482	0.34413	-2777.0773	0.081363	-2777.154137	-2778.642486
INT1'	-2777.451233	0.342676	-2777.0802	0.087621	-2777.161266	-2778.645645
ti-INT3'	-2795.483614	0.511114	-2794.9383	0.095185	-2795.027824	-2797.040988
ti-INT3	-3405.764902	0.684272	-3405.0344	0.123764	-3405.148502	-3408.024217

7.8 References:

Full reference Gaussian 16:

Gaussian 16, Revision B.01, Frisch, M. J.; Trucks, G. W.; Schlegel, H. B.; Scuseria, G. E.; Robb, M. A.; Cheeseman, J. R.; Scalmani, G.; Barone, V.; Mennucci, B.; Petersson, G. A.; Nakatsuji, H.; Caricato, M.; Li, X.; Hratchian, H. P.; Izmaylov, A. F.; Bloino, J.; Zheng, G.; Sonnenberg, J. L.; Hada, M.; Ehara, M.; Toyota, K.; Fukuda, R.; Hasegawa, J.; Ishida, M.; Nakajima, T.; Honda, Y.; Kitao, O.; Nakai, H.; Vreven, T.; Montgomery Jr., J. A.; Peralta, J. E.; Ogliaro, F.; Bearpark, M.; Heyd, J. J.; Brothers, E.; Kudin, K. N.; Staroverov, V. N.; Kobayashi, R.; Normand, J.; Raghavachari, K.; Rendell, A.; Burant, J. C.; Iyengar, S. S.; Tomasi, J.; Cossi, M.; Rega, N.; Millam, J. M.; Klene, M.; Knox, J. E.; Cross, J. B.; Bakken, V.; Adamo, C.; Jaramillo, J.; Gomperts, R.; Stratmann, R. E.; Yazyev, O.; Austin, A. J.; Cammi, R.; Pomelli, C.; Ochterski, J. W.; Martin, R. L.; Morokuma, K.; Zakrzewski, V. G.; Voth, G. A.; Salvador, P.; Dannenberg, J. J.; Dapprich, S.; Daniels, A. D.; Farkas, Ö.; Foresman, J. B.; Ortiz, J. V.; Cioslowski, J.; Fox, D. J. Gaussian, Inc., Wallingford CT, 2016.

(1) Frisch, M. J. .; Trucks, G. W. .; Schlegel, H. B. .; Scuseria, G. E. .; Robb, M. A. .; Cheeseman, J. R. .; Scalmani, G. .; Barone, V. .; Petersson, G. A. .; Nakatsuji, H. .; et al. Gaussian 16, Revision B.01. 2016.

(2)   Becke, A. D. (1993). Density-Functional Thermochemistry. III. The Role of Exact Exchange. J. Chem. Phys. *98*, 5648–5652.

(3)   Lee, C., Yang, W., Parr, R. G. (1988). Development of the Colle-Salvetti Correlation-Energy Formula into a Functional of the Electron Density. Phys. Rev. B *37*, 785–789.

(4)   Vosko, S. H., Wilk, L., Nusair, M. (1980). Accurate Spin-Dependent Electron Liquid Correlation Energies for Local Spin Density Calculations: A Critical Analysis. Can. J. Phys. *58*, 1200–1211.

(5)   Stephens, P. J., Devlin, F. J., Chabalowski, C. F., Frisch, M. J. (1994). Ab Initio Calculation of Vibrational Absorption and Circular Dichroism Spectra Using Density Functional Force Fields. J. Phys. Chem. *98*, 11623–11627.

(6)   Grimme, S., Antony, J., Ehrlich, S., Krieg, H. (2010). A Consistent and Accurate Ab Initio Parametrization of Density Functional Dispersion Correction (DFT-D) for the 94 Elements H-Pu. J. Chem. Phys. *132*, 154104.

(7)   Weigend, F., Ahlrichs, R. (2005). Balanced Basis Sets of Split Valence, Triple Zeta Valence and Quadruple Zeta Valence Quality for H to Rn: Design and Assessment of Accuracy. Phys. Chem. Chem. Phys. *7*, 3297–3305.

(8)   Marenich, A. V., Cramer, C. J., Truhlar, D. G. (2009). Universal Solvation Model Based on Solute Electron Density and on a Continuum Model of the Solvent Defined by the Bulk Dielectric Constant and Atomic Surface Tensions. J. Phys. Chem. B *113*, 6378–6396.

(9)   Grimme, S. (2012). Supramolecular Binding Thermodynamics by Dispersion-Corrected Density Functional Theory. Chem. Eur. J. *18*, 9955–9964.

(10)   Luchini, G., Alegre-Requena, J. V., Funes-Ardoiz, I., Paton, R. S. (2020). GoodVibes: Automated Thermochemistry for Heterogeneous Computational Chemistry Data. F1000Research *9*, 291.

(11)   Contreras-García, J., Johnson, E. R., Keinan, S., Chaudret, R., Piquemal, J. P., Beratan, D. N., Yang, W. (2011). NCIPLOT: A Program for Plotting Noncovalent Interaction Regions. J. Chem. Theory Comput. *7*, 625–632.

(12)   Schrödinger, L. (2015) *The PyMOL Molecular Graphics Development Component, Version 1.8*.

(13)   Abe, H., Shuto, S., Matsuda, A. (2001). Highly α- and β-Selective Radical *C*-Glycosylation Reactions Using a Controlling Anomeric Effect Based on the Conformational Restriction Strategy. A Study on the Conformation - Anomeric Effect - Stereoselectivity Relationship in Anomeric Radical Reactions. J. Am. Chem. Soc. *123*, 11870–11882.

(14)   Adak, L., Kawamura, S., Toma, G., Takenaka, T., Isozaki, K., Takaya, H., Orita, A., Li, H. C., Shing, T. K. M., Nakamura, M. (2017). Synthesis of Aryl *C*-Glycosides via Iron-Catalyzed Cross Coupling of Halosugars: Stereoselective Anomeric Arylation of Glycosyl Radicals. J. Am. Chem. Soc. *139*, 10693–10701.